Multiresolution MR elastography using nonlinear inversion

M. D. J. McGarry[a)]
Thayer School of Engineering, Dartmouth College, Hanover, New Hampshire 03755

E. E. W. Van Houten
Department of Mechanical Engineering, University de Sherbrooke, Sherbrooke, Quebec J1K 2R1, Canada

C. L. Johnson and J. G. Georgiadis
Department of Mechanical Science and Engineering, University of Illinois at Urbana-Champaign, Urbana, Illinois 61801 and Beckman Institute for Advanced Science and Technology, University of Illinois at Urbana-Champaign, Urbana, Illinois 61801

B. P. Sutton
Department of Bioengineering, University of Illinois at Urbana-Champaign, Urbana, Illinois 61801 and Beckman Institute for Advanced Science and Technology, University of Illinois at Urbana-Champaign, Urbana, Illinois 61801

J. B. Weaver
Department of Radiology, Dartmouth-Hitchcock Medical Center, Lebanon, New Hampshire 03755 and Thayer School of Engineering, Dartmouth College, Hanover, New Hampshire 03755

K. D. Paulsen
Thayer School of Engineering, Dartmouth College, Hanover, New Hampshire 03755 and Norris Cotton Cancer Center, Dartmouth-Hitchcock Medical Center, Lebanon, New Hampshire 03755

(Received 27 June 2012; revised 6 September 2012; accepted for publication 6 September 2012; published 1 October 2012)

Purpose: Nonlinear inversion (NLI) in MR elastography requires discretization of the displacement field for a finite element (FE) solution of the "forward problem", and discretization of the unknown mechanical property field for the iterative solution of the "inverse problem". The resolution requirements for these two discretizations are different: the forward problem requires sufficient resolution of the displacement FE mesh to ensure convergence, whereas lowering the mechanical property resolution in the inverse problem stabilizes the mechanical property estimates in the presence of measurement noise. Previous NLI implementations use the same FE mesh to support the displacement and property fields, requiring a trade-off between the competing resolution requirements.
Methods: This work implements and evaluates multiresolution FE meshes for NLI elastography, allowing independent discretizations of the displacements and each mechanical property parameter to be estimated. The displacement resolution can then be selected to ensure mesh convergence, and the resolution of the property meshes can be independently manipulated to control the stability of the inversion.
Results: Phantom experiments indicate that eight nodes per wavelength (NPW) are sufficient for accurate mechanical property recovery, whereas mechanical property estimation from 50 Hz *in vivo* brain data stabilizes once the displacement resolution reaches 1.7 mm (approximately 19 NPW). Viscoelastic mechanical property estimates of *in vivo* brain tissue show that subsampling the loss modulus while holding the storage modulus resolution constant does not substantially alter the storage modulus images. Controlling the ratio of the number of measurements to unknown mechanical properties by subsampling the mechanical property distributions (relative to the data resolution) improves the repeatability of the property estimates, at a cost of modestly decreased spatial resolution.
Conclusions: Multiresolution NLI elastography provides a more flexible framework for mechanical property estimation compared to previous single mesh implementations. © *2012 American Association of Physicists in Medicine*. [http://dx.doi.org/10.1118/1.4754649]

Key words: MR elastography, finite element, viscoelastic, inverse problems

I. INTRODUCTION

Magnetic resonance elastography (MRE) is an emerging medical imaging technique that produces quantitative maps of the mechanical properties of tissue. Tissue shear modulus is relevant to diagnosing diseases including cancer,[1] liver fibrosis,[2] and multiple sclerosis.[3] Other mechanical properties such as the viscoelastic loss modulus[3–5] have also shown promise as diagnostic criteria.

Two common methodologies are available for producing mechanical property estimates from the time-harmonic displacement data measured in MRE. Direct inversion techniques (DI) (Refs. 6–10) pre-filter and differentiate the data to produce a linear system of equations in terms of

the unknown shear modulus. This solution is calculated using numerical estimates of the displacement derivatives in a locally homogeneous version of the governing mechanical equations of motion, and is similar to spatial wavelength estimation.[11] Nonlinear inversion techniques (NLI) (Refs. 12–14) invoke a computational model of the mechanical motion of heterogeneous tissue (the forward problem), and iteratively estimate a set of mechanical property parameters that best reproduces the measured displacements (the inverse problem).

The most commonly applied mechanical model in MRE inversion algorithms is viscoelasticity, where the stiffness is defined by a complex-valued shear modulus, μ. Images of the storage modulus, $\mathrm{Re}\{\mu\}$, have been found to be the most successful indicators of disease to date, with promising *in vivo* results having been reported for breast,[9,15] liver,[2,16] and brain.[17,18] Estimation of alternative mechanical parameters is also possible. For example, estimates of the loss modulus, $\mathrm{Im}\{\mu\}$, improved the specificity of breast cancer diagnosis,[4,19] and contrast has been observed in normal pressure hydrocephalus;[5] however, the loss modulus has been less successful in other applications.[15,18,20] Other alternative mechanical property parameters which have been suggested as imaging candidates include the ratio of transverse anisotropy,[9,21] Rayleigh damping composition,[22] and poroelastic hydraulic conductivity.[23] Producing accurate images of these alternative properties have stronger requirements on data quality, for instance the breast studies[9,15] produced useful loss modulus estimates when increased data SNR was achieved with an improved actuator design. Previous attempts to image alternative mechanical properties have deployed the same spatial resolution as the storage modulus, even though these images are more challenging to produce and may need to be generated at lower spatial resolution to stabilize the inversion estimates and reduce the data SNR required to produce quantitatively accurate values.

This work implements NLI MRE based on independent spatial discretizations for each material property estimate, so that each estimated property is supported with a separate finite element (FE) basis function expansion and concomitant FE mesh. As a result, the degrees of freedom (and hence resolution) associated with each material property parameter is independent of both the data resolution and the computational discretization for the displacement field calculation. The resolution of each estimated mechanical property can be chosen based on other factors such as the expected scale of heterogeneity, parameter sensitivity, and data SNR. An additional benefit of this multiresolution approach is that the mesh resolution of the forward problem does not affect the number of estimated properties. FE methods for the elastodynamic forward problem have requirements on the number of nodes per wavelength for accuracy and convergence. Low stiffness materials at higher actuation frequencies have short shear wavelengths, and forward problem mesh convergence (i.e., to reduce continuum discretization error introduced by the FE approximations) can be assured in these cases by using a fine displacement mesh without compromising the inverse problem.

II. METHODS

II.A. Nonlinear inversion overview

NLI poses the elastographic inverse problem as an iterative minimization of the objective function

$$\Phi(\theta) = \sum_{i=1}^{N_m} \{(u_{m(i)} - u_{c(i)}(\theta))(u_{m(i)} - u_{c(i)}(\theta))^*\}, \quad (1)$$

where $u_{m(i)}$ represents the complex-valued amplitude of the ith displacement measurement, $u_{c(i)}(\theta)$ is the analogous displacement calculated with the forward computational model based on the current estimate of the properties, θ, N_m is the number of measurements and * represents the complex conjugate. The minimization is performed by updating θ using the conjugate gradient method. Calculation of $u_c(\theta)$ is referred to as the "forward problem", and the process of iteratively estimating the material properties that minimize (1) is the "inverse problem". Regularization is usually necessary to stabilize the inversion; spatial filtering[24] and total variation minimization[25] are commonly applied.

The forward problem for NLI techniques requires solution of a partial differential equation (PDE) describing the mechanical motion, which requires boundary conditions (BCs) to be applied around the exterior of the problem domain. In the case of MRE, measured displacements are available throughout the tissue; therefore, Dirichlet fixed displacement BCs can be enforced on any conceivable boundary within the data acquisition volume, which enables a subzone method.[12] Subzone methods reduce the computational load of NLI by solving the inverse problem on a number of smaller subregions of data in parallel. The global distribution of the mechanical property estimates is then assembled from the union of subregion solutions.

Because of discretization error, a PDE has well-characterized resolution requirements for achieving an accurate solution on finite elements. Figure 1 shows the displacement mesh convergence for solution of the inhomogeneous Navier's equation on 27 node quadratic hexahedral

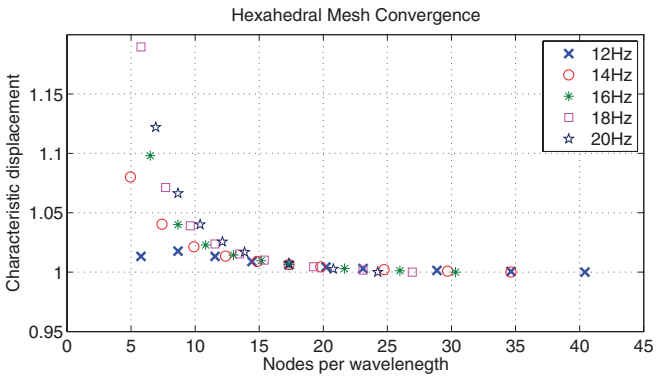

FIG. 1. Hexahedral displacement mesh convergence. The slope of the convergence curve flattens out around 15–20 nodes per wavelength. These curves were generated using a 0.1 m cubic geometry with type 1 shear displacement BCs applied to the bottom face. The characteristic displacement was the absolute value of one of the top corners, the value at the highest resolution was normalized to 1.

finite elements. Presumably, the effect of discretization error is relatively small if it is less than the measurement error in the MRE displacements. MRE noise is approximately 5%, and as Fig. 1 suggests, 12 nodes per wavelength (NPW) produces errors around 2.5%. An estimate of the shear wavelength, L_s, is given by

$$L_s = \frac{1}{f}\sqrt{\frac{\mu}{\rho}}, \tag{2}$$

where f is the actuation frequency. *In vivo* MRE typically operates in the range of 50–100 Hz, and tissue shear modulus is often between 1.5 and 4 kPa. Displacement measurements are commonly acquired with a resolution near 2 mm, which yields measurements per wavelength ranging from 6 to 20. Thus, if a computational mesh resolution is used which is comparable to the measurement resolution, discretization errors may be substantial, especially in softer tissues at higher actuation frequencies.

NLI methods presented in the literature[12,13,22] have supported the unknown mechanical properties on the same finite element mesh as the displacements calculated in the forward problem, which is typically at the same resolution as the displacement data. This approach has produced promising results, however, it trades-off mesh resolution in the forward problem with maintenance of a manageable number of estimated mechanical property estimates.

II.B. Finite element multiresolution implementation

The heterogeneous form of the time-harmonic Navier's equation which describes the evolution of the displacement fields in a viscoelastic material is given by

$$\nabla \cdot (\mu(\nabla\vec{u} + \nabla\vec{u}^T)) + \nabla(\lambda\nabla\cdot\vec{u}) = -\rho\omega^2\vec{u}, \tag{3}$$

where μ is the complex-valued viscoelastic shear modulus, λ is the second Lamẽ parameter, ρ is the density, ω is the excitation frequency, ^{T} represents tensor transposition, and $\vec{u}$ is the complex-valued displacement vector which is computed during solution of the forward problem. In this formulation, the estimated material properties are the storage modulus, $\mathrm{Re}\{\mu\}$, and the loss modulus, $\mathrm{Im}\{\mu\}$. A large value of λ is used together with a stabilized incompressible finite element solution of Eq. (3) to model a nearly incompressible material.[26] The imaginary component of λ is set to zero because attenuation of the long wavelength compressional wave is assumed to be negligible at the scale of MRE problems. ρ is held constant at the density of water.

A subzone based multiresolution NLI algorithm was coded in FORTRAN to run on a distributed computing cluster. Different basis function expansions (and concomitant finite elements and meshes) were used to support the displacements and heterogeneous mechanical properties:

Displacement mesh: Twenty-seven node quadratic hexahedral elements support the displacements because higher order elements achieve mesh convergence at lower nodal densities compared to their linear element counterparts, which can substantially reduce the computational overhead of the forward problem.

Property meshes: Material properties do not need to be supported on high order elements (especially in tissues where the spatial variation is considered to be slow varying except for jump changes at interfaces between tissue types), therefore, eight-node linear hexahedra represent the heterogenous material properties. Separate bases and meshes of independent resolutions were created for the real and imaginary components of each complex-valued mechanical property.

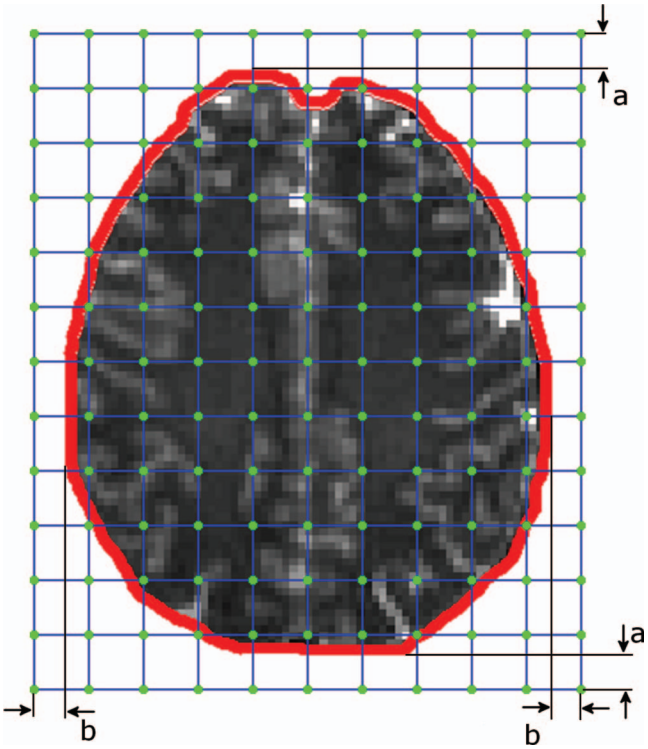

FIG. 2. Two-dimensional illustration of the placement of the material property mesh. The boundary of the global geometry is shown in red, and the material elements are shown as blue lines with green nodes. The material property mesh is placed so that the top/bottom and left/right overlap with the displacement mesh (represented by *a* and *b*, respectively) are equal.

The nodes in these meshes were arranged in a rectangular grid mirroring the structure of MRI data. The displacement mesh was created directly from masked MRE displacement measurements. The displacements were interpolated to the desired computational mesh resolution through a masked cubic spline technique where the nodes of hexahedral displacement elements were created at the interpolated voxel locations. Element with all nodes falling within the mask were included in the global displacement mesh. The forward problem requires property distributions over the whole domain; therefore, the property meshes were sized to overlap the complete displacement mesh as illustrated in Fig. 2.

The forward problem uses Gaussian integration to assemble the finite element stiffness matrix;[26] therefore, the property mesh influences the forward problem by providing values at the displacement element Gauss points (GPs). Solving the

inverse problem on a subzone updates the property values at every property mesh node which affects at least one subzone GP. Therefore, a multiresolution subzone consists of a cluster of displacement elements and all of the property mesh elements that contain subzone displacement element GPs. The global property solution is then constructed by weighting the overlapping subzone property estimates by the number of affected GPs, so that the global property value at node i in the property mesh is given by

$$\theta_g(i) = \frac{1}{N_{Gtot}(i)} \sum_{sz=1}^{N_{sz}} \theta_{sz}(i) N_{Gsz}(i), \tag{4}$$

where $\theta_g(i)$ and $\theta_{sz}(i)$ are the global and subzone property values, respectively, N_{sz} is the number of subzones, $N_{Gsz}(i)$ is the number of displacement GPs affected by node i in subzone sz, and $N_{Gtot}(i) = \sum_{sz=1}^{N_{sz}} N_{Gsz}(i)$. This update weighting reduces the influence of a subzone update for material element that contains very few subzone displacement GPs, which is desirable because property inversion on the subzone will have low sensitivity to changes in the nodal property values of that property mesh element. Other overlapping subzone solutions containing the element will be more sensitive to the nodal property estimates, and be assigned a higher relative weight in the global property description. Property nodes with zero sensitivity ($N_{Gtot}(i) = 0$ because all elements containing property node i are outside the displacement mesh) are not updated. After estimation, property values are interpolated back to the MR measurement voxel location for display and analysis.

II.C. Data collection

A phantom was constructed from porcine skin gelatin (type A, 300 bloom, Sigma-Aldrich; St Louis, MO), with background and inclusion concentrations of 5% and 10% by weight, respectively. Mechanical testing with a TA Instruments Q800 dynamic mechanical analyzer (TA Instruments, New Castle, DE) and time-temperature superposition[27] produced estimates of 3.3 ± 0.8 and 8.8 ± 0.9 kPa for the storage modulus of the background and inclusion materials, respectively (shear wavelengths of the background and inclusion materials at 100 Hz are approximately 18 mm and 30 mm, respectively). Phantom dimensions were approximately $120 \times 65 \times 40$ mm with a conical inclusion of 23 mm base and 100 mm height. The phantom was actuated from below at 100 Hz using a pneumatic system driven by two 16-inch subwoofers powered by an amplified signal generator. Displacement data was collected using a Philips 3T Achieva scanner (Philips Medical Systems Best, The Netherlands) with a single-shot, spin-echo echo-planar imaging sequence modified for MRE with motion sensitizing gradients.[14] Imaging parameters included 1400/40 ms repetition/echo times; 140 mm field-of-view; 80×80 acquired data matrix; 1.8 mm slice thickness (with 0.2 mm gap); 20 slices. Imaging was repeated with motion sensitization along three separate gradient axes, and eight dynamics were acquired over a single period of vibration.

Brain data was also collected on a healthy 24-year-old male volunteer using a Siemens 3T Allegra scanner (Siemens Medical Solutions; Erlangen, Germany). The actuator employed was similar to the head rocker system described by Sack *et al.*,[18] and motion was applied at 50 Hz. Imaging was performed using a multishot, variable-density, spin-echo spiral MRE sequence[28,29] with the following parameters: 6 k-space interleaves; 2000/55 ms repetition/echo times; 256 mm field-of-view; 128×128 acquired data matrix; 2 mm slice thickness; 20 axial slices. As with the phantom, imaging was repeated for all three coordinate directions to acquire full vector field displacements in time. Data was collected using this volunteer on six separate occasions to investigate the reproducibility of the mechanical property estimates. One dataset was discarded because the shear strain SNR was below the threshold of 3.0 required for accurate property recovery.[30]

II.D. Experiment 1: Effect of displacement mesh resolution

The significance of errors caused by insufficient resolution in the displacement mesh has not been carefully quantified in NLI elastography because mesh refinement has not been possible without an accompanying increase in the number of estimated mechanical property parameters. Using the multiresolution approach with gelatin phantom data, the displacement mesh resolution was varied between 5 and 18 NPW in the background material (based on independent DMA stiffness estimates), while holding the viscoelastic parameter mesh resolution fixed at the MRE data resolution. Visual assessment of the inclusion boundary definition and the smoothness of the homogenous property regions provided a qualitative evaluation of the accuracy of the estimated properties over the range of displacement mesh resolutions considered. Manual segmentation of the inclusion based on the MR magnitude image was used to determine the average estimated stiffness for the background and inclusion.

II.E. Experiment 2: Trade-offs between runtime and accuracy by controlling the displacement mesh resolution

The displacement mesh resolution directly impacts the computational time for 3D finite element problems. *In vivo* MRE is typically performed at frequencies around 50 Hz to minimize shear wave attenuation, yielding reasonably long shear wavelengths in many tissue types. Longer shear wavelengths are less susceptible to discretization error; hence, computational speedup may be possible without compromising the quality of the estimated mechanical property images. Runtime reduction through coarse displacement mesh utilization was investigated by estimating *in vivo* brain mechanical properties using displacement mesh resolutions ranging from 1.5 mm to 3 mm, and identifying the point where the estimated property distribution begins to be affected. For these experiments, the resolution of the property meshes was fixed at the data resolution. A property distribution, θ, calculated with displacement mesh resolution, R, is denoted by θ_R.

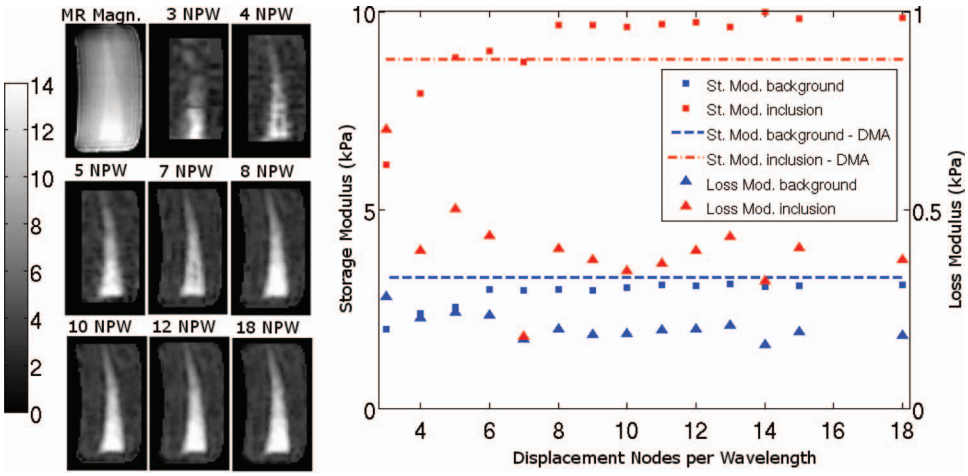

FIG. 3. Effect of displacement mesh resolution on NLI gelatin phantom mechanical property estimates. A typical cross section of the storage modulus image (in kPa) is shown on the left for a range of NPW in the displacement mesh. The background and inclusion were manually segmented based on the MR magnitude image to produce the average values of storage and loss modulus (right). Independent DMA storage modulus estimates of the phantom materials at 100 Hz are shown (dashed lines), and have numerical values of 3.3 ± 0.8 kPa for the background and 8.8 ± 0.9 kPa for the inclusion.

Taking the finest resolution estimation, $\theta_{1.5mm}$, as a reference, the property difference, $\Delta\theta_R$, was defined as

$$\Delta\theta_R = \frac{\overline{\theta_{1.5mm} - \theta_R}}{\overline{\theta_{1.5mm}}} \times 100, \quad (5)$$

where the overbar denotes the mean of all estimated mechanical property parameter values shared between the two datasets. The value of $\Delta\theta_R$ was tabulated along with the relative runtime change compared to setting the displacement resolution equal to the data resolution. Representative images generated at each displacement resolution provided a qualitative comparison.

II.F. Experiment 3: Effect of mechanical property parameter subsampling

In this experiment, the resolutions of the estimated storage and loss moduli were varied between 2 mm and 4 mm, which covered a range from the full data resolution to its reduction by a factor of 2. The effect of these changes on the repeatability of the *in vivo* brain property estimates was investigated. Pixel-by-pixel variation was calculated by rigidly registering the five brain datasets based on T2-weighted images and finding the standard deviation in each common voxel across the datasets. The mean of the standard deviation of the mechanical property estimates for the voxels present in all datasets was used to quantify the variation in each property estimate of the same tissue for each set of property mesh resolutions. Regularization parameters were lowered as much as possible to isolate effects due to changes in the property resolution; smoothing techniques such as spatial filtering are sensitive to the property mesh resolution and can obscure the effect of a change in property mesh resolution. The displacement mesh resolution was held at the MRE data acquisition resolution, resulting in a well-resolved mesh with approximately 16 NPW based on the average brain tissue storage modulus.

III. RESULTS

III.A. Experiment 1: Effect of displacement mesh resolution

Figure 3 shows the averaged shear modulus estimate in the inclusion and background when the displacement mesh resolution is increased while holding the mesh resolution of the estimated mechanical property parameters constant. A qualitative comparison is also provided in terms of typical image cross sections of the storage modulus for a range of NPW for the displacement mesh.

III.B. Experiment 2: Trade-offs between runtime and accuracy by controlling the displacement mesh resolution

Table I and Fig. 4 present *in vivo* image data that result when the displacement mesh resolution is decreased for mechanical property estimation in the brain. Table I compares the

TABLE I. Percentage difference in storage and loss moduli in the brain *in vivo* when the displacement mesh resolution is decreasing. Property resolution is held constant at the data resolution. The property difference is based on using the property estimates generated with a 1.5 mm displacement mesh resolution as a reference [see Eq. (5)] and the runtime is relative to when the displacement mesh resolution is equal to the data resolution.

Displacement resolution (mm)	Approximate NPW	Storage Modulus difference (%)	Loss Modulus difference (%)	Relative runtime
1.52	21	10.7	12.0	2.46
1.6	20	9.65	10.9	2.32
1.7	19	11.5	13.2	1.65
1.8	18	13.4	15.0	1.14
2.0	16	13.2	14.1	1.00
2.2	15	17.2	20.4	0.61
2.5	13	17.4	18.0	0.49
3.0	11	23.3	28.5	0.20
4.0	8	32.8	38.9	0.12

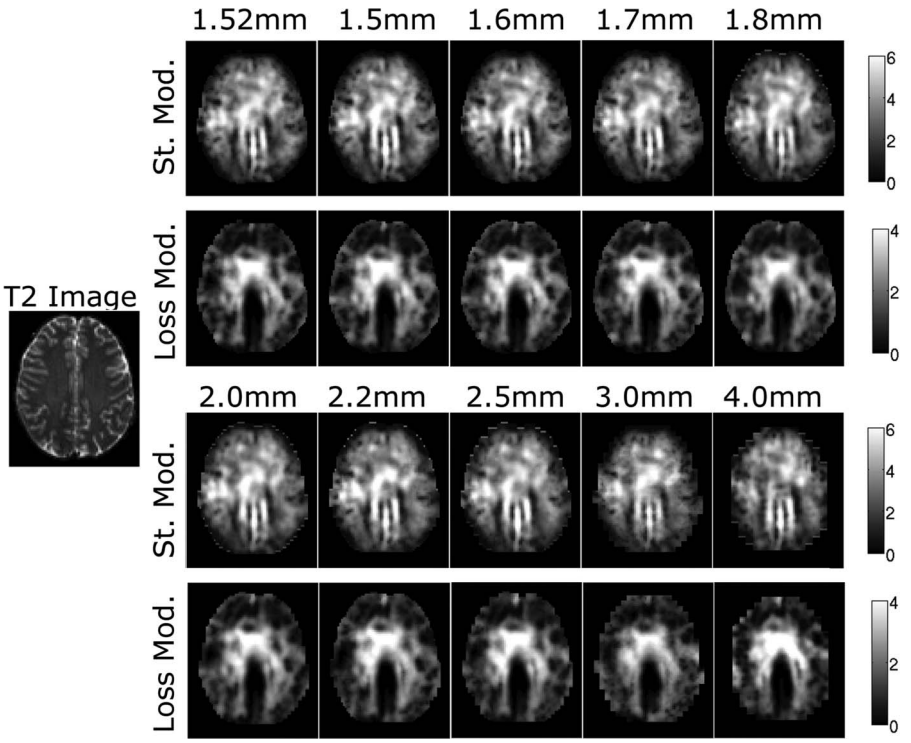

FIG. 4. Typical image cross section of *in vivo* brain mechanical property estimates demonstrating the effect of modifying the displacement mesh resolution. The property mesh resolution was held constant at the resolution of the measured displacements. The storage and loss modulus are shown in separate rows, in units of kPa. The resolution of the displacement mesh used to estimate of each set of mechanical properties is indicated above the images.

percentage differences in storage and loss modulus as well as runtime, whereas Fig. 4 shows a representative image cross section recovered at each displacement mesh resolution.

III.C. Experiment 3: Effect of mechanical property parameter subsampling

Figure 5 contains viscoelastic brain mechanical property estimates over a range of property mesh resolutions. The first 3 columns show the effect of varying the loss modulus resolution while holding the storage modulus resolution fixed, and the fourth and fifth columns indicate the effect of subsampling both parameters at the same time.

Table II reports the pixel-by-pixel variations in mechanical property estimates from five brain imaging sessions involving the same healthy volunteer after rigid registration based on the T2-weighted anatomical images from each scan.

IV. DISCUSSION

Finite element methods require adequate displacement mesh resolution for accurate solution of the discretized

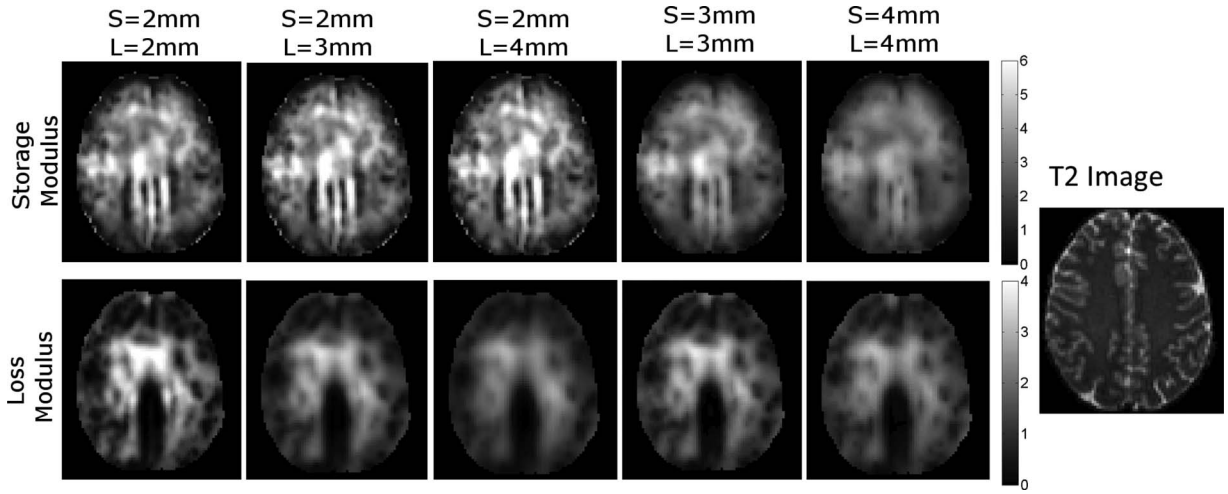

FIG. 5. Typical image cross section from *in vivo* brain data demonstrating the effect of subsampling the storage and loss modulus. Each column shows a single estimate computed using the resolution indicated for the storage modulus (S) and loss modulus (L). Units are kPa.

TABLE II. Mean of pixel-by-pixel variation from five scans of the same healthy volunteer, after rigid registration using the T2-weighted images from each exam, for a range of storage modulus (S) and loss modulus (L) property mesh resolutions. These values are higher than the typical variability of NLI property estimates because regularization was decreased as much as possible to isolate the effect of the property resolution.

Property mesh resolution (mm)	Storage modulus variation (%)	Loss modulus variation (%)
S=2, L=2	23.8	26.9
S=2, L=3	23.8	22.0
S=2, L=4	23.9	19.7
S=3, L=3	19.5	21.7
S=4, L=4	17.9	19.4

partial differential equation (PDE) describing the assumed mechanical motion in tissue. In the case of dynamic elasticity, the number of s is a common measure of mesh refinement. As NPW increases, the finite element discretization error decreases quadratically (assuming linear finite element basis functions), and the FE solution approaches the true solution as the mesh length scales are decreased. On the other hand, the stability of the inverse problem is influenced by the ratio of the number of independent high-SNR measurements to the number of unknown mechanical property parameters to be estimated (larger values of this ratio, M/U, are generally more stable). The number of measurements is essentially fixed based on imaging time and SNR constraints. Indeed, most clinical MRE studies measure displacement data at a resolution of 2–3 mm. The M/U ratio can be controlled by altering the resolution of the estimated parameters through their associated mesh discretizations. Supporting the displacements and mechanical properties on the same basis functions (i.e., mesh) forces a compromise between the competing requirements of displacement mesh convergence (displacement discretization error approaching zero) and inverse problem stability (increasing M/U). Developing a multiresolution approach provides a more flexible framework for NLI MRE, and simultaneously allows displacement mesh convergence and inverse problem stability to be optimized independently.

Figure 1 indicates that the short shear wavelength of soft materials when excited at higher frequencies can require a displacement mesh resolution much finer than the data resolution to achieve low discretization error. The finite element displacement and mechanical property discretizations appearing in previous single mesh NLI implementations were not sufficient to allow displacement mesh refinement with no consequence to inverse problem stability, whereas the new multiresolution approach provides independent control of displacement NPW. The results in Fig. 3 indicate that the inversion accuracy is not affected until the mesh resolution is lower than 8 NPW, where Fig. 1 predicts discretization errors on the order of 5%. At lower resolution, the discretization errors become substantial and begin to degrade the inversion. However, even at very poor resolution approaching 5 NPW, the inversion retains reasonable quantitative accuracy, and a qualitative assessment of the property images suggests that the errors are generally confined to local artifacts and loss of inclusion boundary definition. These results are promising for NLI MRE because they imply that the larger computational burden of using a very fine displacement mesh is not critical to recover accurate mechanical property estimates.

Experiment 2 indicates the displacement mesh resolution is more important for *in vivo* data where fine scale mechanical property variation is present. Table I shows that the property difference stabilizes around 10%–12%, once the displacement mesh resolution reaches 1.7 mm (or 19 NPW based on the mean brain storage modulus). This property difference is an expression of the uncertainty in the NLI property estimates at the SNR of our current MRE brain data. No continuum mechanical model is a perfect representation of tissue behavior – model-data mismatch and discretization of continuum displacement and material property fields contribute to *in vivo* modelling errors. Refining the displacement mesh resolution reduces the computational discretization error; however, small changes in the location of the subzone boundaries and material property nodes alter the model-data mismatch and its effect on the inversion, which contributes to this base level of pixel-by-pixel mechanical property uncertainty.

Using a 1.7 mm displacement mesh comes at a cost of a 65% increase in computational time compared to setting the displacement mesh resolution equal to the data resolution of 2 mm. However, using a displacement mesh resolution of 3.0 mm reduces runtime by 80% and still maintains much of the spatial mechanical property information captured by estimates generated using a high resolution displacement mesh. Thus, the extra runtime for high displacement mesh resolution could be compensated by using a coarse displacement resolution for earlier NLI iterations to provide an improved initial property estimate for inversion using a high resolution displacement mesh, so that fewer high resolution iterations are ultimately required.

Multiresolution MRE allows independent control of the resolutions of the real and imaginary components of each mechanical property parameter, which has not been possible previously. Figure 5 shows that subsampling the loss modulus while holding the storage modulus resolution fixed has little effect on the storage modulus image, but stabilizes the loss modulus estimates at a modest cost of lower resolution. This suggests that parameters which are traditionally more difficult to estimate (such as the loss modulus) can be subsampled to stabilize the inversion without influencing parameters which can be successfully estimated (imaged) at high resolution (such as the storage modulus). Subsampling both parameters simultaneously smooths and stabilizes both property estimates. Table II indicates that the variation of a parameter decreases with subsampling due to the regularization effect of decreasing the number of unknowns in the inversion. The loss modulus has typically proven to be the more difficult viscoelastic parameter to estimate accurately. Using a coarser property mesh resolution may allow more robust loss modulus estimates while retaining high resolution storage modulus images. A moderate reduction in estimated mechanical property resolution will reduce the visibility of small scale mechanical property variations; however, many of the

clinical MRE results reported to date have used a spatial average of mechanical properties taken over large regions.[2,5,17,31] A moderate reduction in the property resolution will not have a large effect on these types of measurements.

The sensitivity of the displacements, u, to changes in a parameter, θ, is described by $\frac{\partial u}{\partial \theta}$. Lower sensitivity parameters are typically more difficult to estimate from the data; however, the difference in quality of the storage and loss moduli estimates is not solely a function of sensitivity, because $\frac{\partial u}{\partial \mathrm{Im}\{\mu\}} = i\frac{\partial u}{\partial \mathrm{Re}\{\mu\}}$. A more likely explanation is model-data mismatch. The storage modulus may better describe the elastic effects in tissue compared to the loss modulus model of attenuation, which suggests the loss modulus values do not reflect physical characteristics of tissue as well as the storage modulus. More complicated material models such as poroelasticity and anisotropic elasticity may be more appropriate for tissue, which should decrease model-data mismatch; however, in these cases additional unknown parameters are introduced that must be estimated from the same data. The sensitivity difference between parameters in these complicated models may be large, for example, tissue displacements are more sensitive to changes in poroelastic shear modulus compared to changes in hydraulic conductivity. The multiresolution framework is expected to be valuable in these cases, where low sensitivity parameters can be supported on a coarse mesh to allow more accurate estimation (albeit at lower resolution).

Additionally, MRE applications with low SNR (such as the lung[32]) may benefit from reducing the number of unknown parameters in the inversion by deploying a coarser material property resolution for all mechanical parameters.

V. CONCLUSIONS

The multiresolution approach presented provides a flexible framework for NLI MR elastography. The competing requirements of reducing displacement field discretization error and increasing inverse problem stability can be independently controlled, and each estimated mechanical property parameter can have its own (different) resolution. Phantom experiments suggest that adequate displacement mesh resolution occurs above eight nodes per wavelength, although initial *in vivo* results indicate that this value is likely closer to 20 NPW. Results from a viscoelastic implementation also indicate that changing the loss modulus resolution has little effect on the storage modulus images, and the pixel-by-pixel repeatability of *in vivo* brain mechanical property estimates increases with the regularizing effect of subsampling. Subsampling parameters which are more difficult to estimate may produce more robust quantitative estimates without degrading the resolution of mechanical property estimates that are already robust (such as the storage modulus). The parameter resolution can also be selected based on the SNR of the motion data, and property estimation from noisy displacement measurements may be stabilized by sacrificing resolution for a decrease in the number of unknown mechanical property parameters in the inversion.

ACKNOWLEDGMENTS

The development of the multiresolution NLI algorithm was supported by a grant from the National Institutes of Health (Grant No. R01CA159324-02). Collection of brain MRE data was supported by the Biomedical Imaging Center at the Beckman Institute for Advanced Science and Technology, University of Illinois at Urbana-Champaign.

[a]Electronic mail: matthew.d.mcgarry@dartmouth.edu

[1]A. Samani, J. Zubovits, and D. Plewes, "Elastic moduli of normal and pathological human breast tissues: An inversion-technique-based investigation of 169 samples," Phys. Med. Biol. **52**(6), 1565–1576 (2007).
[2]L. Huwart *et al.*, "Magnetic resonance elastography for the noninvasive staging of liver fibrosis," Gastroenterology **135**(1), 32–40 (2008).
[3]J. Wuerfel, F. Paul, B. Beierbach, U. Hamhaber, D. Klatt, S. Papazoglou, F. Zipp, P. Martus, J. Braun, and I. Sack, "MR-elastography reveals degradation of tissue integrity in multiple sclerosis," Neuroimage **49**(3), 2520–2525 (2010).
[4]R. Sinkus, K. Siegmann, T. Xydeas, M. Tanter, C. Claussen, and M. Fink, "MR elastography of breast lesions: Understanding the solid/liquid duality can improve the specificity of contrast-enhanced MR mammography," Magn. Reson. Med. **58**(6), 1135–1144 (2007).
[5]K.-J. Streitberger, E. Wiener, J. Hoffmann, F. B. Freimann, D. Klatt, J. Braun, K. Lin, J. McLaughlin, C. Sprung, R. Klingebiel, and I. Sack, "In vivo viscoelastic properties of the brain in normal pressure hydrocephalus," NMR Biomed. **24**(4), 385–392 (2010).
[6]A. Manduca, T. E. Oliphant, M. A. Dresner, J. L. Mahowald, S. A. Kruse, E. Amromin, J. P. Felmlee, J. F. Greenleaf, and R. L. Ehman, "Magnetic resonance elastography: Non-invasive mapping of tissue elasticity," Med. Image Anal. **5**(4), 237–254 (2001).
[7]T. E. Oliphant, A. Manduca, R. L. Ehman, and J. F. Greenleaf, "Complex-valued stiffness reconstruction for magnetic resonance elastography by algebraic inversion of the differential equation," Magn. Reson. Med. **45**, 299–310 (2001).
[8]R. Sinkus, J. Lorenzen, D. Schrader, M. Lorenzen, M. Dargatz, and D. Holz, "High-resolution tensor MR elastography for breast tumour detection," Phys. Med. Biol. **45**(6), 1649–1664 (2000).
[9]R. Sinkus, M. Tanter, S. Catheline, J. Lorenzen, C. Kuhl, E. Sondermann, and M. Fink, "Imaging anisotropic and viscous properties of breast tissue by magnetic resonance elastography," Magn. Reson. Med. **53**, 372–387 (2005).
[10]S. Papazoglou, U. Hamhaber, J. Braun, and I. Sack, "Algebraic helmholtz inversion in planar magnetic resonance elastography," Phys. Med. Biol. **53**, 3147 (2008).
[11]A. Manduca, "Characterization and evaluation of inversion algorithms for MR elastography," Proc. SPIE **4684**, 1180–1185 (2002).
[12]E. E. W. Van Houten, M. I. Miga, J. B. Weaver, F. E. Kennedy, and K. D. Paulsen, "Three-dimensional subzone-based reconstruction algorithm for MR elastography," Magn. Reson. Med. **45**, 827–837 (2001).
[13]E. E. W. Van Houten, M. M. Doyley, F. E. Kennedy, K. D. Paulsen, and J. B. Weaver, "A three-parameter mechanical property reconstruction method for MR-based elastic property imaging," IEEE Trans. Med. Imaging **24**, 311–324 (2005).
[14]J. B. Weaver, E. E. W. Van Houten, M. I. Miga, F. E. Kennedy, and K. D. Paulsen, "Magnetic resonance elastography using 3D gradient echo measurements of steady-state motion," Med. Phys. **28**, 311–324 (2001).
[15]R. Sinkus, M. Tanter, T. Xydeas, S. Catheline, J. Bercoff, and M. Fink, "Viscoelastic shear properties of in vivo breast lesions measured by MR elastography," Magn. Reson. Imaging **23**, 159–165 (2005).
[16]R. L. Ehman, "Science to Practice: Can MR Elastography Be Used to Detect Early Steatohepatitis in Fatty Liver Disease?," Radiology **253**(1), 1–3 (2009).
[17]M. C. Murphy, J. Huston, C. R. Jack, K. J. Glaser, A. Manduca, J. P. Felmlee, and R. L. Ehman, "Decreased brain stiffness in alzheimer's disease determined by magnetic resonance elastography," J. Magn. Reson. Imaging **498**, 494–498 (2011).
[18]I. Sack, B. Beierbach, U. Hamhaber, D. Klatt, and J. Braun, "Non-invasive measurement of brain viscoelasticity using magnetic resonance elastography," NMR Biomed. **21**(3), 37–41 (2008).

[19]K. C. Siegmann, T. Xydeas, R. Sinkus, B. Kraemer, U. Vogel, and C. D. Claussen, "Diagnostic value of MR elastography in addition to contrast-enhanced MR imaging of the breast-initial clinical results," Eur. Radiol. **20**(2), 318–25 (2010).
[20]M. A. Green, L. E. Bilston, and R. Sinkus, "In vivo brain viscoelastic properties measured by magnetic resonance elastography," NMR Biomed. **21**(7), 755–764 (2008).
[21]E. C. Qin, R. Sinkus, C. Rae, and L. E. Bilston, "Investigating anisotropic elasticity using MR-elastography combined with diffusion tensor imaging: Validation using anisotropic and viscoelastic phantoms," Proc. Intl. Soc. Mag. Reson. Med. **19**, 39 (2011).
[22]E. E. W. Van Houten, D. vR. Viviers, M. D. J. McGarry, P. R. Perriñez, I. I. Perreard, J. B. Weaver, and K. D. Paulsen, "Subzone based magnetic resonance elastography using a Rayleigh damped material model," Med. Phys. **38**(4), 1993–2004 (2011).
[23]A. J. Pattison, P. R. Perrinez, M. D. J. McGarry, J. B. Weaver, and K. D. Paulsen, "Estimating hydraulic conductivity in vivo using magnetic resonance elastography," Mech. Biol. Syst. Mater. **2**, 41–48 (2011).
[24]E. E. W. Van Houten, K. D. Paulsen, M. I. Miga, F. E. Kennedy, and J. B. Weaver, "An overlapping subzone technique for MR-based elastic property reconstruction," Magn. Reson. Med. **42**, 779–786 (1999).
[25]K. D. Paulsen and H. Jiang, "Enhanced frequency-domain optical image reconstruction in tissues through total-variation minimization," Appl. Opt. **35**(19), 3447–3458 (1996).
[26]O. C. Zienkiewicz and R. L. Taylor, *The Finite Element Method. Vol. 1, The Basis* (Butterworth-Heinemann, Oxford, UK, 2000).
[27]M. M. Doyley, I. Perreard, A. J. Patterson, J. B. Weaver, and K. M. Paulsen, "The performance of steady-state harmonic magnetic resonance elastography when applied to viscoelastic materials," Med. Phys. **37**, 3970–3979 (2010).
[28]C. L. Johnson, M. D. J. McGarry, E. E. W. Van Houten, J. B. Weaver, K. D. Paulsen, B. P. Sutton, and J. G. Georgiadis, "Magnetic resonance elastography of the brain using multishot spiral readouts with self-navigated motion correction," Magnetic Resonance in Medicine (accepted).
[29]C. L. Johnson, M. D. Mcgarry, A. A. Gharibans, J. B. Weaver, K. D. Paulsen, B. P. Sutton, and J. G. Georgiadis, "High-resolution multishot MR elastography of the brain with correction for motion-induced phase errors," Proc. Intl. Soc. Mag. Reson. Med. **20**, 2517 (2012).
[30]M. D. J. McGarry, E. E. W. Van Houten, P. R. Perriñez, A. J. Pattison, J. B. Weaver, and K. D. Paulsen, "An octahedral shear strain-based measure of SNR for 3D MR elastography," Phys. Med. Biol. **56**, N153–N164 (2011).
[31]I. Sack, B. Beierbach, J. Wuerfel, D. Klatt, U. Hamhaber, S. Papazoglou, P. Martus, and J. Braun, "The impact of aging and gender on brain viscoelasticity," Neuroimage **46**(3), 652–657 (2009).
[32]K. P. McGee, R. D. Hubmayr, and R. L. Ehman, "MR elastography of the lung with hyperpolarized 3He," Magn. Reson. Med. **59**(1), 14–18 (2008).